



Grafting Fe(III) species on carbon nanodots/Fe-doped g-C₃N₄ via interfacial charge transfer effect for highly improved photocatalytic performance



Qiong Liu, Tianxiang Chen, Yarong Guo, Zhengguo Zhang, Xiaoming Fang*

Key Laboratory of Enhanced Heat Transfer and Energy Conservation, The Ministry of Education, School of Chemistry and Chemical Engineering, South China University of Technology, Guangzhou 510640, China

ARTICLE INFO

Article history:

Received 8 September 2016
Received in revised form 2 December 2016
Accepted 8 December 2016
Available online 9 December 2016

Keywords:

Photocatalysis
g-C₃N₄
Interfacial charge transfer effect
Carbon nanodots

ABSTRACT

Carbon quantum dots (CQDs) are coupled with Fe-doped g-C₃N₄ to prepare a binary composite photocatalyst, which shows retarded recombination of photo-induced carriers and enhanced surface absorption active sites. Then, interfacial charge transfer effect (IFCT) is introduced the binary composite by grafting Fe(III) species on the surface of CQDs/Fe-doped g-C₃N₄ via a facile impregnation method. The obtained ternary Fe(III)/CQDs/Fe-doped g-C₃N₄ composite photocatalyst exhibits largely increased optical absorption with its absorption region extended to 1200 nm and efficiently inhibited charge recombination through the IFCT effect. It is revealed that the increased surface absorption active sites provided by CQDs lead to more amount of Fe(III) species anchored in the ternary photocatalyst than in the binary Fe(III)/Fe-doped g-C₃N₄ composite, which favors the photocatalytic activity. The EPR probe experiments elucidate that •OH active species could be generated from the ternary Fe(III)/CQDs/Fe-doped g-C₃N₄ photocatalyst under visible light irritation, originating from the cooperation between the IFCT effect and the photo-Fenton reaction due to the existence of the Fe(III) species, which accounts for its highly enhanced photocatalytic performance on the degradation of MO and phenol.

© 2016 Elsevier B.V. All rights reserved.

1. Introduction

Semiconductor-based photocatalysis technology based on the photocatalysts with visible light response and good stability is considered as a promising strategy to solve the energy crisis and environmental contamination issues by utilizing solar energy [1]. Recently, graphitic carbon nitride (g-C₃N₄), serving as a metal-free polymeric organic photocatalyst, has attracted much attention for use in the production of hydrogen via water splitting and the degradation of organic pollutions [2,3], owing to its visible light response, high chemical stability and easy-modified textural structure. However, due to the existence of several drawbacks including the relative narrow visible-light absorption range, fast recombination of photo-induced charge and the weak oxidizing ability, g-C₃N₄ suffers from the relatively low photocatalytic performance and thus limits its practical applications under solar light.

In order to address the inherent limitations in g-C₃N₄, various strategies have been developed, including doping with metal and

nonmetal elements [4], constructing heterojunctions with other semiconductor [5,6], morphology control [7–9] or copolymerization with organic molecules [10], and combination with carbon materials [11]. As one of the important strategies among the modification means, doping with substituent transition metal atoms (Fe [12], Co [13], V [14], et al.) has provided a new class of g-C₃N₄-based photocatalysts with enhanced catalytic activity. This is because g-C₃N₄ possesses the abundant so-called “nitrogen pots”, which are the feasible ideal sites for metal inclusion [15]. Moreover, the incorporation of a carbon material with g-C₃N₄ has been proven to be an attractive method for facilitating charge transfer and increasing the surface active sites [16,17]. Recently, Liu et al. [11] reported that carbon quantum dots (CQDs) coupled g-C₃N₄ exhibited the high quantum efficiency for photocatalytic water splitting owing to the surface-sensitized property by CQDs. And from the theoretical study by Gao et al. [18], it is considered that there would be a type-II van der Waals heterojunction formed between CQDs and g-C₃N₄, where CQDs serves as a spectral sensitizer to broaden optical absorption and yield more surface active absorption sites. From these results, we are inspired to construct CQDs/Fe-doped g-C₃N₄ composite with enhanced photocatalytic performance by integrating the functions of Fe doping and CQDs coupling. It is rea-

* Corresponding author.

E-mail address: cexmfang@scut.edu.cn (X. Fang).

sonable that the coupling of CQDs with Fe-doped g-C₃N₄ renders the higher oxidized ability, the promoted charge transfer process and the enhanced surface active sites due to the formation of the type-II van der Waals heterojunction at the interface of CQDs/Fe-doped g-C₃N₄.

Furthermore, interfacial charge transfer effect (IFCT) has been examined to be an efficient way to simultaneously enhance the optical absorption region largely and reduce the charge transport distance for photocatalysts [19,20]. Very recently, Our group has constructed a Fe(III) grafted g-C₃N₄ photocatalyst via IFCT, which shows the apparent red-shift of the absorption band edge extending to the whole visible light region along with an obvious absorption peak ranging from 800 to 1200 nm [21]. This is ascribed to the formation of the discrete energy levels between the grafted Fe(III) species and g-C₃N₄, which shortens the electron transportation distance from the valence band of g-C₃N₄ to the surface active sites. The high photocatalytic performance of Fe(III)/g-C₃N₄ demonstrates that IFCT is an efficient modification way to construct high-performance g-C₃N₄-based catalysts.

In the current work, IFCT was employed to develop a ternary Fe(III)/CQDs/Fe-doped g-C₃N₄ photocatalyst by grafting Fe(III) species on the surface of the binary CQDs/Fe-doped g-C₃N₄ composite. Firstly, the CQDs/Fe-doped g-C₃N₄ composite was synthesized by the high temperature thermal polymerization. Then the Fe(III) species were grafted on the surface of the binary via a facile impregnation method. It is found that, the obtained ternary photocatalyst not only exhibited enhanced optical absorption and shorten charge transfer distance, but also formed Fe(III)/Fe(II) with a proper potential for inducing the inner Fenton-like reaction, both of which facilitate photocatalytic reactions.

2. Experimental section

2.1. Sample preparation

2.1.1. Materials

Rapeseed flower bee pollens were supplied from an online store in the Taobao website. Dicyandiamide, ferric chloride (FeCl₃·6H₂O), 5,5-dimethyl-1-pyrroline-N-oxide (DMPO) and 2,2,6,6-tetramethylpiperidinyloxy (TEMPO) were analytical grade and purchased from Sigma Aldrich Chemical Co (Shanghai, China).

2.1.2. Preparation of Fe-doped C₃N₄

Fe-doped C₃N₄ was synthesized according to a reported method [12]. Typically, 30 ml of distilled water was added to a mixture consisting of 4 g of dicyandiamide and different amounts of FeCl₃·6H₂O, followed by adjusting to pH = 2 using 0.06 ml HCl (6 mM). After being thoroughly stirred at 353 K, the mixture was dried. And then the obtained solid was transferred in a muffle furnace followed by being heated to 823 K and maintained for 4 h at a heating rate of 15 K/min. The resultant product was milled into powder and donated as Fe-CN. The mass ratio of FeCl₃·6H₂O to dicyandiamide is set at 0.1, 0.2, 0.5 and 1.0 wt%, respectively. In addition, pristine g-C₃N₄ (donated as pure CN) was obtained under the same condition without the addition of FeCl₃·6H₂O.

2.1.3. Preparation of CQDs

CQDs were obtained from rapeseed flower bee pollen via a hydrothermal method [22]. Briefly, 40 ml of bee pollens (1 g) aqueous suspension was heated at 453 K in a Teflon-lined stainless steel autoclave and stayed for 24 h. After being filtered, a transparent solution of CQDs was obtained.

2.1.4. Preparation of CQDs/Fe-doped C₃N₄

The CQDs/Fe-doped CN composites were prepared by adding different volumes of the CQDs solution into the mixture containing

dicyandiamide (4 g) and 0.2 wt% of FeCl₃·6H₂O, followed by the process identical to the preparation of Fe-CN, in which the CQDs mass fractions were set at 0.15, 0.20, 0.25 and 0.30 wt%, respectively. The obtained samples were donated as CQDs/Fe-CN.

2.1.5. Preparation of Fe(III)/CQDs/Fe-doped C₃N₄

The process for preparing Fe(III)/CQDs/Fe-doped CN is as follows: 0.3 g of the as-made 0.25%-CQDs/Fe-CN was added into 80 ml of deionized water followed by ultrasonically dispersing for 30 min. And then, different amounts of FeCl₃·6H₂O were added into the dispersion solution, followed by adjusting to pH = 2 and stirring at 353 K for 10 h. After natural cooling, the resultant solids were collected by centrifugation, washing and drying at 333 K for 10 h in a vacuum oven.

For comparison purposes, Fe(III)/Fe-doped CN composites were also prepared by incorporation of different amount of FeCl₃·6H₂O onto 0.2%-Fe-CN via the same process.

2.2. Characterization

The morphologies of the prepared samples were observed by a Zeiss Merlin scanning electron microscope (SEM), a FEI Tecnai G20 transmission electron microscopes (TEM). X-ray diffraction (XRD) patterns and infrared absorption spectra were recorded by a Bruker D8 advance diffraction meter and a Bruker Vector 33 Fourier transform infrared (FT-IR) spectrophotometer, respectively. The X-ray photoelectron spectroscopy (XPS) was carried out by a Kratos Axis Ultra DLD system with the excited source of Mg to analyze the chemical bonding information. Elemental analysis of iron content was conducted by using Varian ICP-OES 720. UV/VIS/NIR diffuse reflectance spectra was investigated by a PerkinElmer Lambda 950 UV/VIS/NIR spectrophotometer, and photoluminescence (PL) spectra was observed with a Hitachi F-4600 spectrometer under the 375 nm of excitation wavelength. Specific surface area (BET) was measured by a Micromeritics ASAP 2020 apparatus. Solid electron spin resonance (ESR) signals of the samples were investigated by a Bruker model A300 spectrometer at room temperature. The iron ion concentration is detected by a Titan AFS-9130 Atomic Fluorescence spectrometer. Electrochemical properties were measured by a CHI660E electrochemical workstation with a conventional three-electrode system, in which Pt wire and an Ag/AgCl electrode were served as counter electrode and reference electrode, respectively. Working electrodes were fabricated by coating a pastes onto the FTO glass using the doctor-blading method, followed by annealing at 423 K for 2 h. The pastes were prepared by mixing 0.1 g of each catalyst with 0.01 g ethyl cellulose in 10 ml ethanol solution, followed by grinding.

2.3. Evaluation of photocatalytic activity

Methylene orange (MO) and phenol were selected as the model contaminants to evaluate the photocatalytic activity of the obtained samples under visible-light irradiation, which is generated by a 300W Xe lamp with a 420 nm cutoff filter. Briefly, 50 mg of each catalyst was dispersed into 100 ml of MO solution (10 mg/L). Prior to illumination, the suspension solution was stirred for 30 min to ensure the adsorption-desorption equilibrium in a darkroom. At given 10 min interval, about 3 ml aliquots was collected and centrifuged at 10000 rpm for 10 min to gain the clear MO solution. This supernatant was subsequently measured by a Shimadzu UV-2050 UV-vis spectrophotometer. The procedure for the degradation of phenol was carried out under the same condition as that for MO. For identifying the products generated from the photodegradation of MO, liquid chromatography-mass spectrometry (LC-MS) was conducted, which was equipped with a Zorbax C18 column (150 × 4.6 mm i.d., 5 μm). Several trap agents including

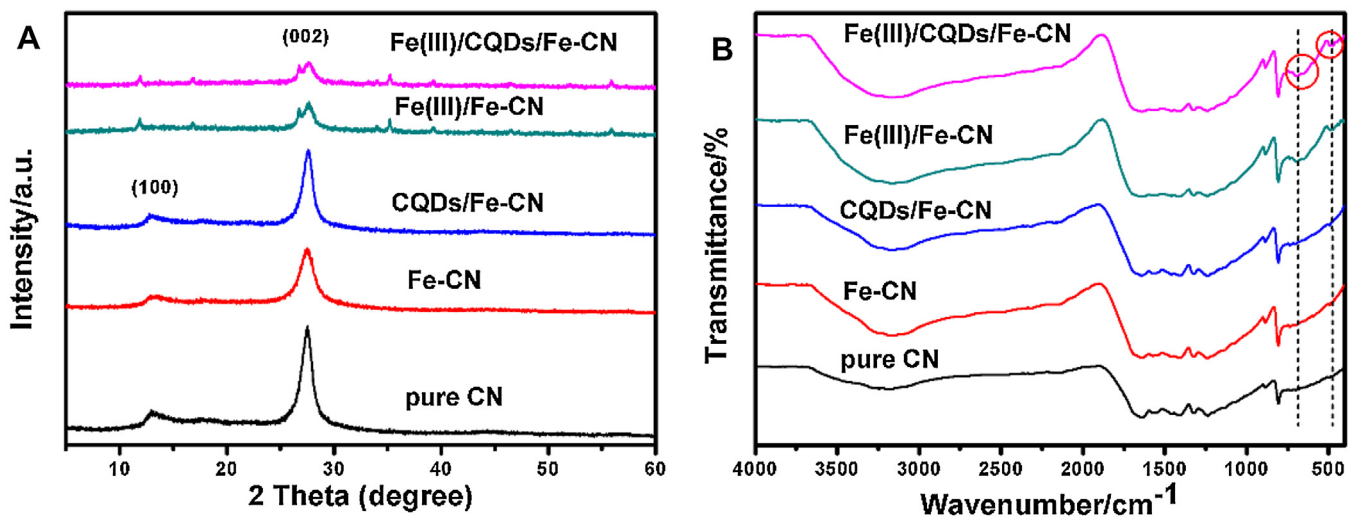


Fig. 1. XRD pattern (A) and FT-IR spectra (B) of pure CN, 0.2%-Fe-doped CN, 0.25%-CQDs/Fe-doped CN, 8%-Fe(III)/Fe-CN, 8%-Fe(III)/CQD/Fe-CN.

benzoquinone (BQ), isopropanol (IPA) and ammonium oxalate (AO) were added into the model pollution solution during the photocatalytic reaction to trap superoxide radicals ($O_2^{\bullet-}$), hydroxyl radicals ($\bullet OH$) and holes (h^+), respectively, in which the 8%-Fe(III)/CQDs/Fe-CN catalyst was dispersed. Additionally, electron spin resonance (ESR) signals of the reactive oxygen species were examined by the probe molecule 5, 5-dimethyl-1-pyrroline-N-oxide (DMPO) and 2, 2, 6, 6-tetramethylpiperidinyloxy (TEMPO).

3. Results and discussion

3.1. Structure and morphology

XRD patterns of pure CN, Fe-CN, CQDs/Fe-CN, Fe(III)/Fe-CN and Fe(III)/CQD/Fe-CN are shown in Fig. 1A. Both pure CN, Fe-CN and CQDs/Fe-CN show two similar distinct diffraction peaks at 13.2° (100) and 27.5° (002), which corresponding to in-plane tri-s-thiazine repeating motifs and the interlayer reflection of the graphitic like structure [23]. The absence of the diffraction peaks for CQDs over CQDs/Fe-CN might be ascribed to the low content of CQDs. For the Fe(III)/Fe-CN and Fe(III)/CQD/Fe-CN samples, the typical (002) peak at 27.5° is also found, indicating the crystal structure of g-C₃N₄ mainly keeps unchanged, but the peak located at 13.2°

is absent. Moreover, several new diffraction peaks can be observed from the XRD patterns of Fe(III)/Fe-CN and Fe(III)/CQD/Fe-CN. More detailed information can be seen from Fig. S1 that these new peaks would be indexed to FeOOH (JCPDS No. 421315), demonstrating the iron ion is transformed into FeOOH during preparation by the impregnation method [24]. And the absence of the peak at 13.2° might be ascribed to the FeOOH species grafted onto the surface which partly weakens the diffraction peaks presence of g-C₃N₄. As displayed in Fig. 1B, pure CN, Fe-CN, CQDs/Fe-CN, Fe(III)/Fe-CN and Fe(III)/CQD/Fe-CN show the typical FT-IR spectrum of g-C₃N₄. The broad band located at 3000–3600 cm⁻¹ is mainly ascribed to the N–H stretching vibration, several strong peaks ranging from 1800 to 1200 cm⁻¹ are indexed to C–N heterocycles skeletal vibration of the aromatic (C₆N₇) ring. And the intense peak at 807 cm⁻¹ is corresponded to the out-of-plane stretching vibration of the characteristic triazine cycles [21]. While, note that two other new peaks presented at 475, 694 cm⁻¹ over Fe(III)/Fe-CN and Fe(III)/CQD/Fe-CN are attributed to Fe–O bonding, which belongs to the formed FeOOH [25].

To identify the chemical states of Fe(III)/CQD/Fe-CN, XPS technology was employed. Five elements including C, N, O, Fe, Cl are observed in the survey spectrum (Fig. 2A). Comparing to pure CN, Fe(III)/CQD/Fe-CN shows the similar typical characteristic C and N

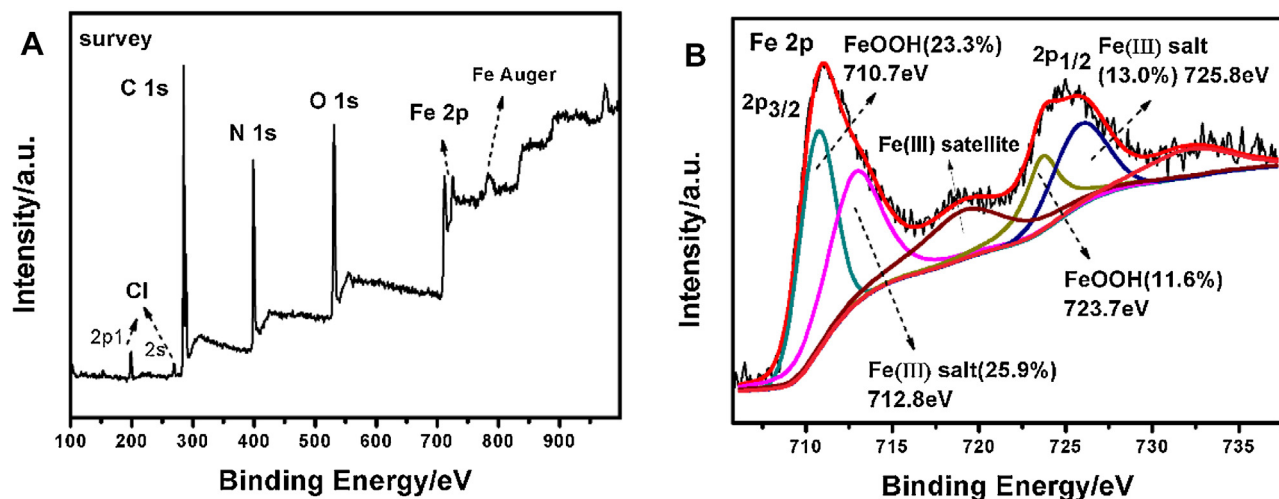


Fig. 2. XPS spectra of survey (A) and Fe 2p (B) over 8%-Fe(III)/CQD/Fe-CN composite.

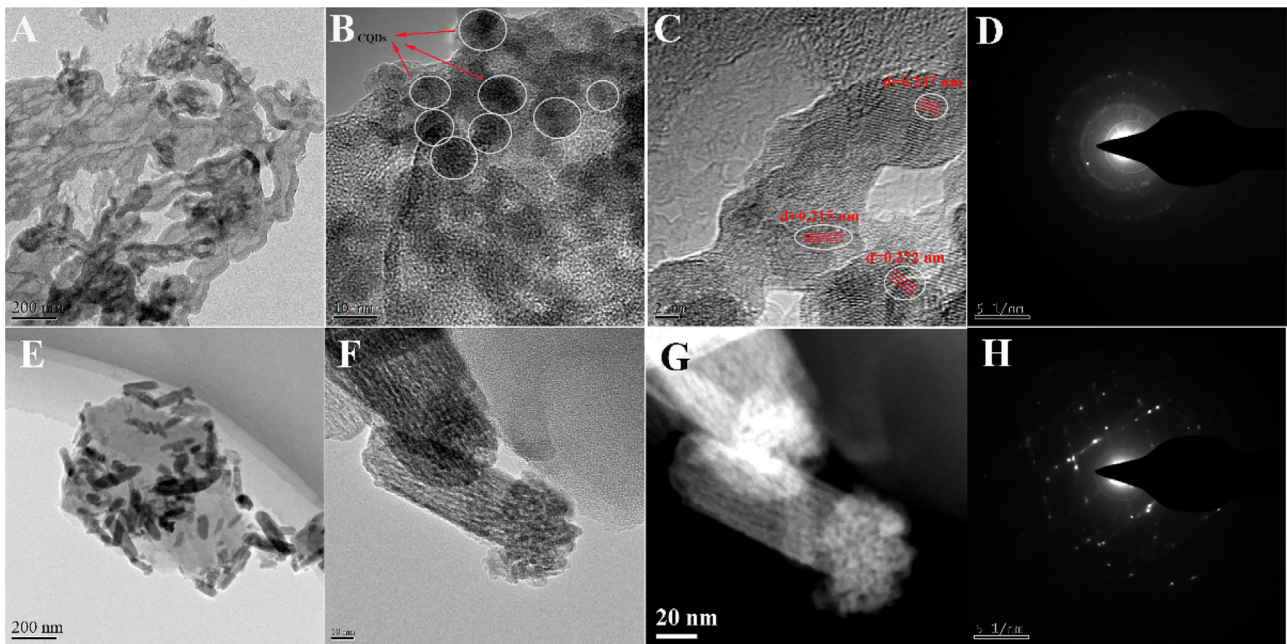


Fig. 3. TEM images of 0.25%-CQDs/Fe-doped CN (A–D), 8%-Fe(III)/CQD/Fe-CN (E–H), picture (G) correspond to STEM images of picture (F), selected area electron pattern (SAED) of 0.25%-CQDs/Fe-doped CN (D) and 8%-Fe(III)/CQD/Fe-CN (H).

peaks, as revealed from the high resolution C 1 s and N 1 s spectra in Fig. S2, in which three C 1 s peaks located at 284.6, 285.1, 288.6 eV are ascribed to C–C, C–N, C=O, respectively, and the peaks in the N 1 s spectrum at 398.9, 399.7, 401.1 eV are derived from pyridinic-N, C=N–C, and N-(C)₃, respectively [26]. While with regards to the O 1 s spectrum in Fig. S2(C), apart from the two peaks belonging to C–O (531.2 eV) and C=O (532.3 eV), there also presents a new broad peak at 529.7 eV which it is not observed in pure CN. These peaks can be ascribed to the Fe=O bonding, which are originated from FeOOH [27]. This is in accord with the aforementioned FT-IR results. In addition, compared to pure CN, Fe(III)/CQD/Fe-CN exhibits the two C–O and C=O peaks at the lower binding energies, as shown in Fig. S2(C). These might be ascribed to the Fe=O bonding alters the outer layer valence electron density of oxygen atom, which decreases the binding energy of C–O bonding [28,29]. For the high resolution Fe 2p spectrum in Fig. 2B, Fe 2p_{3/2} can be deconvoluted into three peaks including 710.7 eV for FeOOH, 712.8 eV for the residual Fe(III) salt and 719.3 eV for Fe (III) satellite peak [30]. The existence of residual Fe(III) salt accounts for the presence of Cl element in the survey spectrum, which originates from FeCl₃. Comparisons in Fe 2p spectrum among Fe-CN, CQDs/Fe-CN, Fe(III)/Fe-CN and Fe(III)/CQD/Fe-CN are shown in Fig. S3. For Fe-CN and CQDs/Fe-CN, the relatively weak peaks of Fe could be found, demonstrating the successful incorporation of Fe into CN network. When referred to Fe(III)/Fe-CN, its Fe 2p spectrum is similar to that of Fe(III)/CQD/Fe-CN, indicating the same chemical bonding states of Fe element in the two composites. Moreover, the Fe content in pure CN, 0.2%-Fe-CN, 0.25%-CQDs/Fe-CN, 8%-Fe(III)/Fe-CN and 8%-Fe(III)/CQDs/Fe-CN was measured by ICP-OES, and the obtained results were listed in Table S1. The weight fraction of Fe in 0.2%-Fe-CN and 0.25%-CQDs/Fe-CN is about 0.19% and 0.16%, respectively, close to their nominate contents, indicating that Fe has been doped into g-C₃N₄. While about 6.12% and 8.28% of Fe is detected in 8%-Fe(III)/Fe-CN and 8%-Fe(III)/CQD/Fe-CN, the former of which is lower than its nominate content, and the latter is close to the nominate one. Furthermore, Fe(III)/Fe-CN and Fe(III)/CQD/Fe-CN with different nominate contents of Fe (III) were prepared by adding different amounts of FeCl₃ during the preparation, and their weigh fractions of Fe were measured by

ICP-OES. As shown in Fig. 4S, when the nominate addition content of Fe is less than 6%, the weigh fractions of Fe in the resulted samples are very close to their corresponding nominate contents. While, at the Fe nominate content of 8%, the weigh fraction of Fe in Fe(III)/Fe-CN is less than that in Fe(III)/CQD/Fe-CN, which is lower than its nominate content of 8%, indicating that the existence of CQDs help to the grafting of the Fe(III) species. As the nominate content of Fe is increased to 10%, the weigh fraction of Fe does not increase accordingly. This result might be due to the limited surface absorption active sites in CN framework that suppress the more content of FeOOH grafted into the surface [31]. In addition, after the preparations of 8%-Fe(III)/Fe-CN and 8%-Fe(III)/Fe-CN completed, their residual supernatant solutions were collected and analyzed by atomic fluorescence spectrometer. The iron ion concentration is detected to be 62 mg/L in the residual supernatant solution for 8%-Fe(III)/Fe-CN and 12 mg/L in that for 8%-Fe(III)/CQDs/Fe-CN, further confirming that the incorporation of CQDs would generate more active absorption sites for grafting FeOOH.

TEM images of pure CN and Fe-CN are shown in Fig. S5, compared to pure CN with a typical bulk two-dimension layer network, Fe-CN exhibits the similar layer structure but consists of many pores in the microstructure, which might originate from a trace amount of gas release from FeCl₃·6H₂O under the high temperature copolymerization process. Fig. S6 shows the HRTEM image of pure CQDs, it would be found that the obtained CQDs is uniformly distributed in aqueous solution and retains a relative small size ranged from 2 nm to 5 nm. After incorporation CQDs into Fe-CN (Fig. 3), the relatively black dots which refer to the CQDs are observed in the surface of Fe-CN. HRTEM image in Fig. 3C shows CQDs that retains three different lattice distance including 0.215, 0.237, 0.272 nm and from the SAED pattern, three bright diffraction rings could be clearly found, demonstrating the high crystallization of CQDs and well coupled with Fe-CN. For Fe(III)/CQD/Fe-CN in Fig. 3E–F, it is obviously found that many nanorods with different size anchor into the surface and from the STEM image in Fig. 3G, it confirms the nanorods are indexed to the Fe species. Additionally, from the SEM image in Fig. S7, it is also observed Fe species with the rods shape graft in the CN surface and SEM-EDS element mapping analysis of Fe element in Fig. S8 further reveals FeOOH

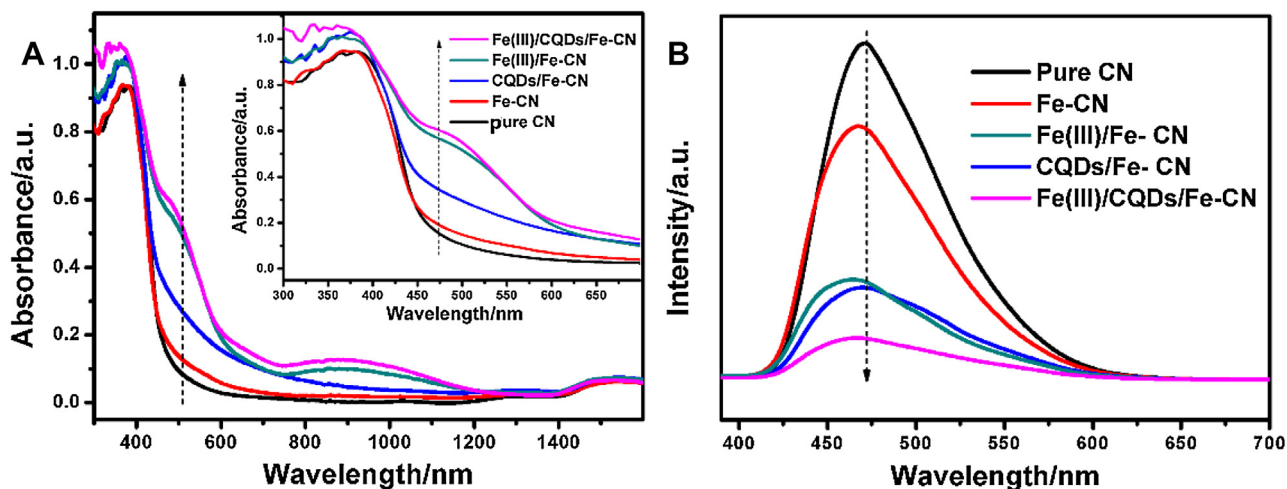


Fig. 4. UV-VIS-NIR spectrum (A) and photoluminescence (PL) emission spectra (B) of pure CN, 0.2%-Fe-doped CN, 0.25%-CQDs/Fe-doped CN, 8%-Fe(III)/Fe-CN, 8%-Fe(III)/CQD/Fe-CN composites (The excitation wavelength is 375 nm).

are uniformly distributed. For comparison, similar size and shape of FeOOH particles over Fe(III)/Fe-CN are also presented in Fig. S9. Furthermore, SAED pattern (Fig. 3H) is carried out that shows bright diffraction spots over Fe(III)/CQD/Fe-CN sample, demonstrating the high crystallinity of FeOOH, which is consistent of the XRD results. In order to illustrate the difference of specific surface area, the N_2 sorption-desorption isotherms of the obtained samples are conducted in Fig. S10 and Table S1. All of the samples just exhibit a relative small specific surface area (SSA), the SSA of Fe(III)/CQD/Fe-CN is $17.51\text{ m}^2/\text{g}$ which is about 2.06 folds of pure CN. And the pore volume over Fe(III)/CQD/Fe-CN is measured to $0.074\text{ cm}^3/\text{g}$, which is larger than other samples, suggesting a relatively faster transfer rate of charge carriers.

3.2. Optical properties

In order to evaluate optical absorption property, UV-VIS-NIR spectrum of the resulted materials was conducted in Fig. 5A. Compared to pure CN, Fe-CN presents a slightly blue shift of the intrinsic absorption edge, this may be due to the he quantum confinement resulted of the holey microstructure. And the enhancement

absorption region from 450 to 600 nm is contributed to the iron complexation via the inclusion iron doped into the CN framework [23]. For CQD/Fe-CN, the absorption edge is almost maintained unchanged but an obvious extension of the visible light absorption region among 450–700 nm can be found. This result mainly due to the photosensitization by CQDs, as the $\pi-\pi$ conjugation CQDs could serve as a photosensitizer which just likes the organic dyes to sensitize Fe-CN under optical excitation. And then it donates the excited electron to the coupled material, resulting in the increase of visible light response region [22]. While, after incorporation of Fe(III) into Fe-CN, the absorption edge of the Fe(III) Fe-CN exhibits a clearly red shift and the light absorption intensity is much enhanced over the whole visible light region, indicating the grafted Fe(III) species into the surface would effectively facilitate the optical absorption property. Notably, it can be observed an obvious absorption peak presents from 760 to 1200 nm, revealing the optical absorption spectrum of Fe(III)/Fe-CN could extend to the near-infrared region and the similar result is also investigated by our previous report [21]. It is ascribing to the IFCT effect that one part of the excited electron from valence band (VB) of CN could directly transfer to the surface Fe(III) species instead of the conduction band

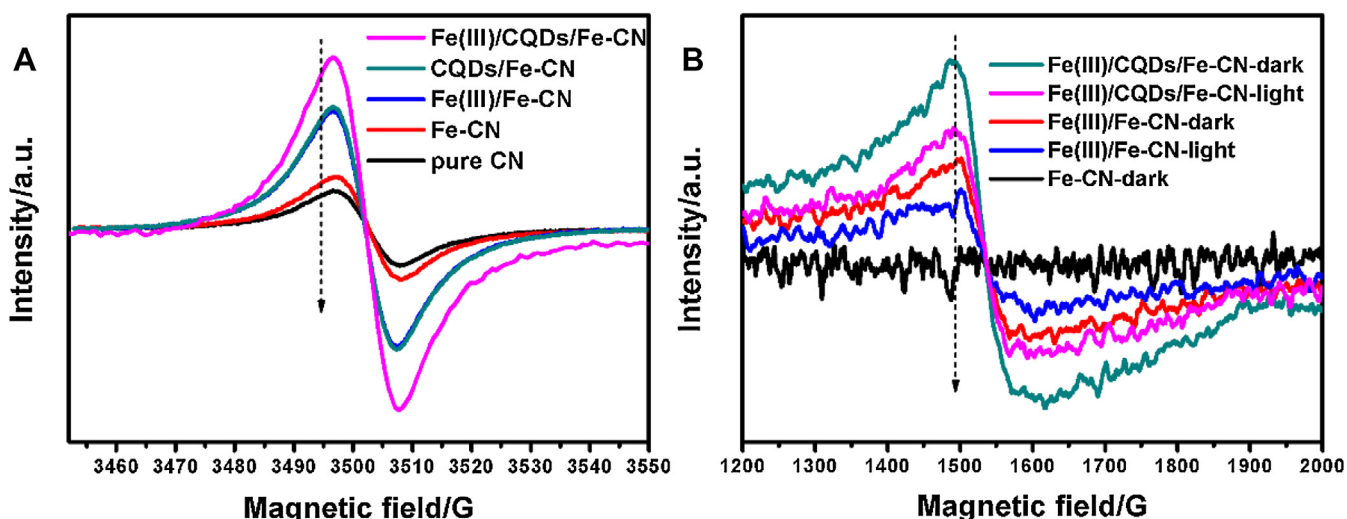


Fig. 5. Room-temperature Solid-state EPR spectra of electron (A) for pure CN, 0.2%-Fe-doped CN, 0.25%-CQDs/Fe-doped CN, 8%-Fe(III)/Fe-CN, 8%-Fe(III)/CQD/Fe-CN composites in the dark, low temperature (100 K) EPR spectra of Fe^{3+} (B) for 0.2%-Fe-doped CN, 8%-Fe(III)/Fe-CN, 8%-Fe(III)/CQD/Fe-CN measured with visible light ($\lambda > 420\text{ nm}$) or in the dark under atmospheric conditions.

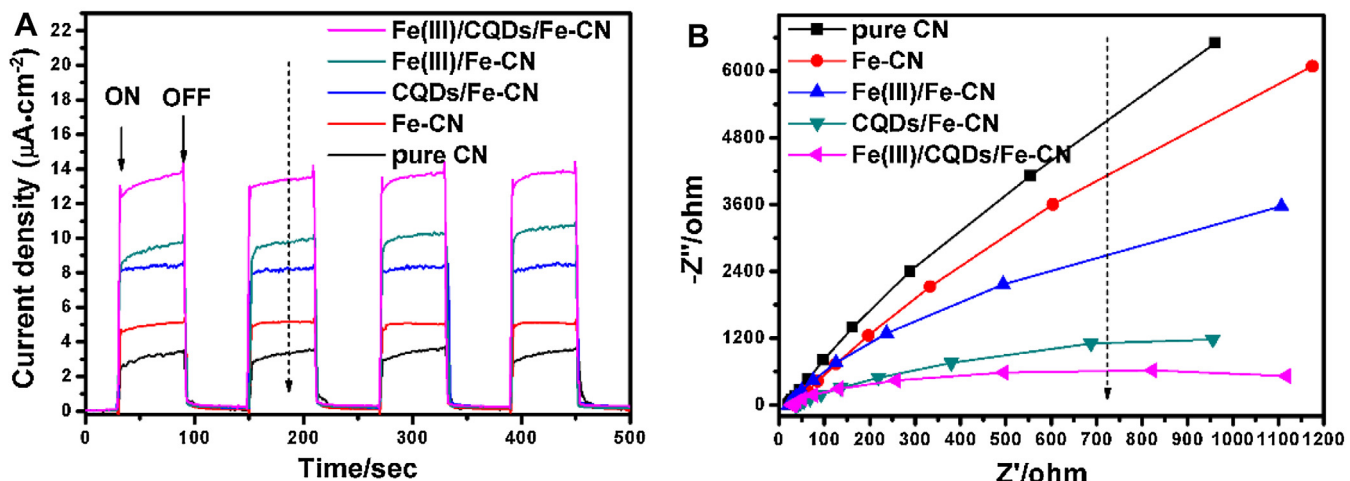


Fig. 6. Photoelectrochemical properties of pure CN, 0.2%-Fe-doped CN, 0.25%-CQDs/Fe-doped CN, 8%-Fe(III)/Fe-CN, 8%-Fe(III)/CQD/Fe-CN. (A) Periodic ON/OFF photocurrent response in 0.2 M Na_2SO_4 electrolyte under visible light irradiation ($\lambda > 420 \text{ nm}$) at 0.5 V vs. Ag/AgCl electrode and (B) electrochemical impedance spectroscopy (EIS) Nyquist plots in the dark.

[24,32,33]. When refers to the energy difference between VB of CN to Fe(III)/Fe(II) (0.77 V, vs SHE pH = 0) is less than 1.0 V, much decrease than the band gap of CN (2.67 V), which resulting in largely reduction of the charge transportation distance. As a consequence, combined the IFCT effect by grafted Fe(III) and photosensitization by CQDs, Fe(III)/CQDs/Fe-CN renders the largest optical absorption region among the other obtained samples.

Fig. 4B shows the photoluminescence (PL) spectra to investigate the photo-induced charge recombination behavior. Compared to pure CN, Fe-CN exhibits the decrease PL intensity, indicating that the appropriate doping amount of Fe into CN could inhibit charge recombination rate. For CQD/Fe-CN composite, it can be observed that an obvious reduced PL intensity occurred, demonstrating the incorporation of CQDs would effectively suppress the recombination of photo-induced carriers. When refers to Fe(III)/Fe-CN, the intensity of PL emission peak is also large reduced, which is contributed to IFCT effect that paves way for efficient delivering of photo-generated electron [34]. The combination of CQDs and Fe(III) into Fe-CN resulted of the unique chemical and optical properties lead to far lower PL intensity of Fe(III)/CQDs/Fe-CN.

Solid electron paramagnetic resonance (EPR) analysis for the prepared samples was performed to examine the electronic band structure and charge transfer in the photocatalysts, as shown in Fig. 5. The single EPR signal at 3502 G ($g = 2.01$) is observed for the samples, which is related to the unpaired electrons originating from the odd numbers of carbon atoms in aromatic rings, indicating a well existent semiconductors framework [35]. After incorporation of CQDs or Fe(III) species, both CQDs/Fe-CN and Fe(III)/Fe-CN show the enhanced EPR signal when compared to Fe-CN. And Fe(III)/CQDs/Fe-CN exhibits larger intensity than all the other samples, implying a greater ability for generating delocalizing spins resulting in the higher charge transfer mobility. Fig. 5B shows the low temperature EPR spectra of Fe-CN, Fe(III)/Fe-CN and Fe(III)/CQDs/Fe-CN at a relative low magnetic field to learn the Fe(III) states as an effect of light irradiation. A signal at 1536 G with a g value of 4.22 is observed for Fe(III)/Fe-CN and Fe(III)/CQDs/Fe-CN in the dark, ascribed to isolated Fe^{3+} containing oxidic clusters located in a strongly distorted monoclinic environment [36]. While no EPR signal is found for Fe-CN, demonstrating Fe is not grafted onto the CN surface, but doped into the crystal structure of CN [37]. This result is well consistent with the aforementioned analysis that the Fe(III) species are confirmed to be the FeOOH -like clusters. Additionally, the signal intensity of Fe^{3+} at $g = 4.22$ is both decreased over Fe(III)/Fe-CN and Fe(III)/CQDs/Fe-CN under light irradiation, it

is deduced that Fe^{3+} is reduced to Fe^{2+} after trapping the photo-induced electrons excited by CN. And as Fe^{2+} ion renders the even of d^6 electron configurations, the EPR signal of Fe^{2+} almost cannot be detected, then leading to the reduced of Fe^{3+} EPR signal [38]. Correspondingly, this conclusion reveals one part of the excited electrons from CN would directly transfer from valence band of CN to the grafted Fe(III) via the IFCT effect and then reduce Fe(III) to Fe(II) under visible light illumination.

Fig. 6 shows the electrochemical results to further investigate the photo-generated charge and the separation of carrier behaviors. From Fig. 6A, as expected, the transient photoelectrochemical response current of both CQDs/Fe-CN and Fe(III)/Fe-CN show a larger value than Fe-CN. And Fe(III)/CQDs/Fe-CN presents the highest current response, which is almost 2.69 and 4.02 folds of Fe-CN and pure CN, respectively. The enlarged photocurrent value of Fe(III)/CQDs/Fe-CN indicates the higher photo-generated charge intensity [39], which is one of the key factors deciding the photocatalytic activity. Moreover, the response photocurrent over photocatalysts samples mostly switch reversibly and unchanged after repeated several ON/OFF illumination cycles, implying the good photoelectrochemical stability. In Fig. 6B, an obvious decrease of semicircular Nyquist plots over Fe(III)/CQDs/Fe-CN is observed, which obeys the order of Fe(III)/CQDs/Fe-CN < CQDs/Fe-CN < Fe(III)/Fe-CN < Fe-CN < pure CN, demonstrating the more efficient separation and transfer efficiency of the photo-induced carriers after the addition of CQDs and the grafted Fe(III) species [40].

3.3. Photocatalytic evolution

The photocatalytic performance of the obtained samples are evaluated by degraded of MO under visible light irradiation, as shown in Fig. 7A. The optimized 0.2%-Fe-CN (Fig. S11) presents a relative small increase of photocatalytic activity (about 33% MO degradation rate in 60 min), compared to pure CN (15% MO degradation). For CQDs/Fe-CN, The photodegradation result of MO over different mass fractions of CQDs coupled with 0.2%-Fe-CN is displayed in Fig. S12, about 55% MO is removed by 0.25%-CQDs/Fe-CN, due to the enhanced visible light absorption region and the retarded recombination of hole-electron pairs. While further raised the CQDs amount, the photodegradation rate is suppressed, as the "shield effect" of CQDs [41]. When grafted Fe(III) into the surface of 0.25%-CQDs/Fe-CN (Fig. S13), it could be clearly seen that the photo-

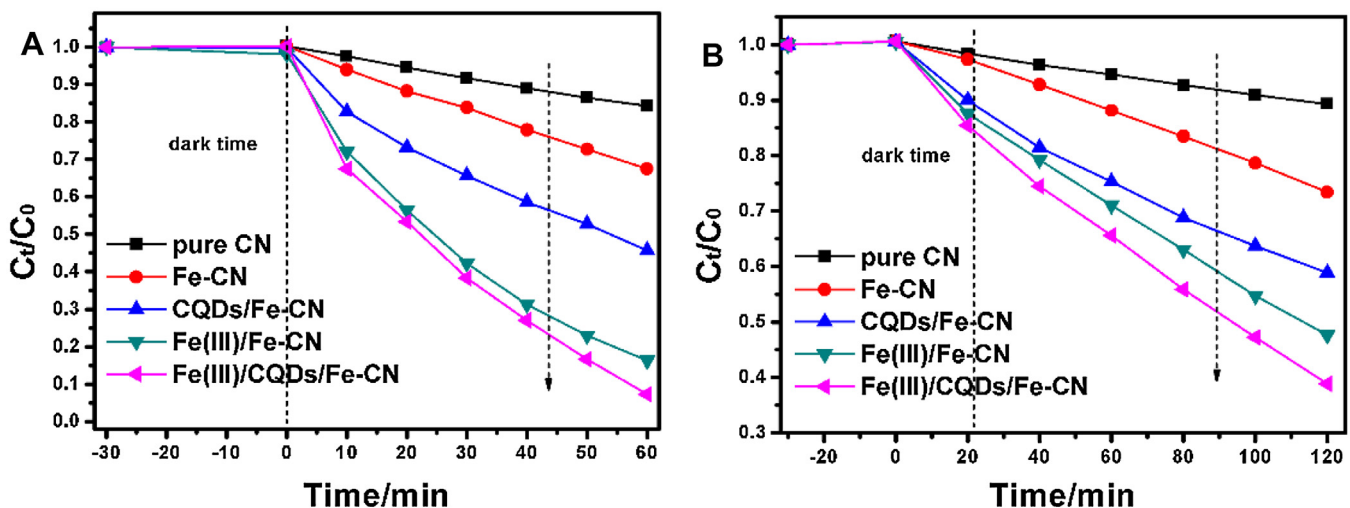


Fig. 7. photocatalytic activity evaluation of pure CN, 0.2%-Fe-doped CN, 0.25%-CQDs/Fe-doped CN, 8%-Fe(III)/Fe-CN, 8%-Fe(III)/CQD/Fe-CN for degradation of (A) MO and (B) phenol under visible light irradiation (>420 nm).

catalytic activity increases with the nominal mass fraction of Fe ion to CQDs/Fe-CN increasing from 2% to 8%, and 8%-Fe(III)/CQDs/Fe-CN composite exhibits the highest photocatalytic activity that about 93% of MO is removed for 60 min. However, further increase the nominal addition amount of Fe ion to 10%, the remove rate of MO does not correspondingly increase. Combined the aforementioned ICP-OES results in Fig. S4, it could be found that the essence grafted Fe(III) mass fraction into the surface almost maintain the same amount among the nominal 8%-Fe(III)/CQDs/Fe-CN and 10%-Fe(III)/CQDs/Fe-CN. This result is mainly due to the limited surface active sites for grafting more amount of Fe(III). The similar result is also found over the different mass fraction of Fe(III) grafted into Fe-CN in Fig. S14, but the Fe(III) species content over Fe(III)/Fe-CN is smaller than Fe(III)/CQDs/Fe-CN when the nominal addition amount is 8% or 10%. This might be contributed to the incorporation of CQDs would promote more active absorption sites for grafting more Fe(III) species. On the other hand, from these results, we would conclude the content of grafted Fe(III) species plays a key role in the photocatalytic performance. Moreover, the colorless substances of phenol is selected as the other model pollutant to further evaluate the photocatalytic performance. From Fig. 7B, pure CN exhibits a relatively low photodegradation efficiency for 120 min (only 10% phenol removed) and a small increase of photodegradation activity is found over Fe-CN. When refers to CQDs/Fe-CN and Fe(III)/Fe-CN, an obvious enhanced of phenol remove rate is observed. After combined CQDs and Fe(III) into Fe-CN, about 71% percent of phenol is removed after 120 min over Fe(III)/CQDs/Fe-CN. And as phenol molecule is consider to be more difficult to be degraded compared to MO, this result further confirms the inherent highly visible light photocatalytic activity of the obtained sample after modification of pure CN.

In other case, in order to investigate the degradation intermediates and residual dye of MO over Fe(III)/CQDs/Fe-CN, LC-MS is conducted and the corresponding mass speak intensity variation with the different irradiation time is shown in Fig. S15. The peak intensity of MO molecule ($m/z = 304$) is decreased rapidly under the visible light illumination and several peaks intensity of consecutive fraction ions among $m/z = 274, m/z = 225, m/z = 214, m/z = 163$ are correspondingly increased, the possible configuration formula of fraction ions are displayed in Fig. S16. Along with the extended irradiation time, some fragment ions are first increased and then decreased gradually, indicating the intermediate products is not stable and could further be decomposed gradually to

the smaller molecule fragment. Finally, the residual by-products present apparently reduced intensity and could completely be degraded to inorganic small molecule to some extent.

Additionally, the photocatalytic stability of Fe(III)/CQDs/Fe-CN was investigated by repeated five times bleach experiment of MO, as shown in Fig. S17, no obvious decline of the photocatalytic activity is observed. And there is also not distinct alteration of crystal structure among fresh and after reaction sample, as examined by XRD and FTIR spectrum in Fig. S18. We further find that no leakage of the iron species in supernatant of MO residual is detected by atomic fluorescence spectrometer after reaction, demonstrating the Fe(III)/CQDs/Fe-CN composite keeps good stability under this applied experiment condition.

3.4. Photocatalytic mechanism

To elucidate the oxidative reaction mechanism, several radical scavenger experiments are carried out on the degradation of MO over Fe(III)/CQDs/Fe-CN in Fig. 8. It is observed that the degradation rate is suppressed when purged N_2 to dump out the dissolved O_2 in the reaction system. And when addition of benzoquinone (BQ), an efficient radical scavengers for $O_2^{\bullet-}$, an obvious inhibition of the decomposition of MO is observed. The generation of active oxygen species $O_2^{\bullet-}$ is confirmed by an EPR/DMPO spin trap technique. In the dark time, no apparent EPR peak is found. However, it can be clearly observed that the characteristic peaks which indexed to the DMPO/ $O_2^{\bullet-}$ adduct with the relative intensity ratio of 1:1:1:1 present in Fig. 8B under visible light irradiation. While it is needed to note that, as $O_2^{\bullet-}$ adduct is a relatively mild oxidant, which could not be completely decomposed MO to the inorganic carbon. In other case, after added isopropanol (IPA) to trap $\bullet OH$, the degradation rate of MO is largely retarded, demonstrating the $\bullet OH$ is the major oxidation species in this photocatalytic system. When carried out the EPR/DMPO trapping experiment, four EPR peaks with the relative intensity of 1:2:2:1 are investigated under visible light illumination, which corresponding to characteristic peaks of DMPO/ $\bullet OH$. When compared to $O_2^{\bullet-}$ adduct, $\bullet OH$ renders the relative stronger oxidizing ability which might decompose the dye or aromatic molecules into carbon dioxide to some extent. The result might elucidate the reason that Fe(III)/CQDs/Fe-CN exhibits the highly photocatalytic activity. In general, as the formation of $\bullet OH/OH^{-1}$ (1.99 eV vs. NHE) is larger than the valence band potential of pure CN (1.57 eV vs. NHE), pure CN almost can-

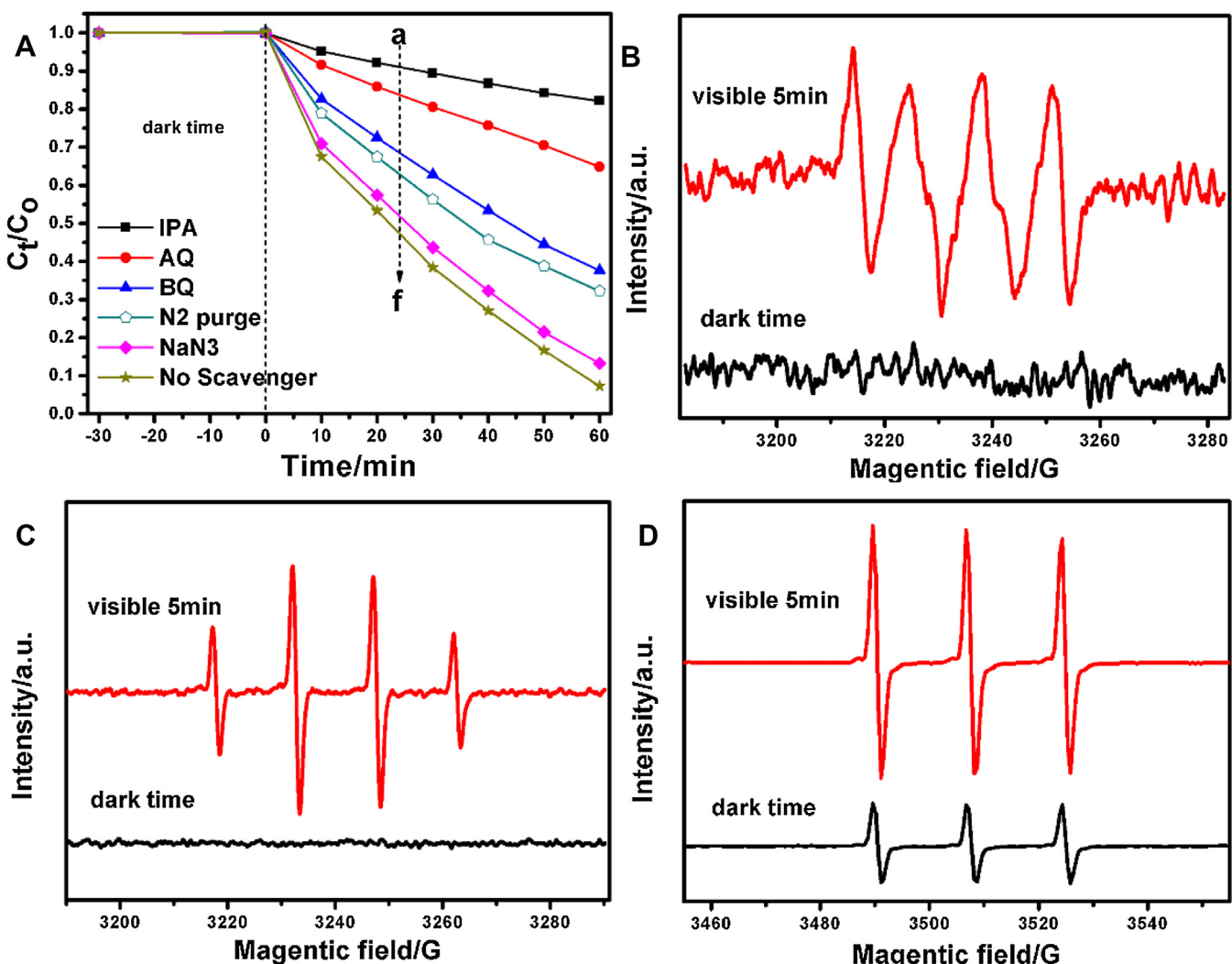
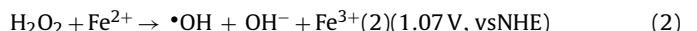
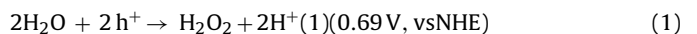


Fig. 8. (A) Time dependent photodegradation of MO over 8%-Fe(III)/CQD/Fe-CN with the addition of different radical scavengers: (a) 10 mM IPA; (b) 10 mM AO; (c) 10 mM BQ; (d) N₂ purge; (e) 10 mM NaN₃; (f) no scavenger addition, ESR spectra of DMPO/*OH (B), DMPO/O₂^{•-} (C) and TEMPO/1O₂ (D) adducts over 8%-Fe(III)/CQD/Fe-CN in aqueous solution before and after 5 min under visible light irradiation ($\lambda > 420$ nm).

not generate *OH adduct under visible light irritation [42]. And the EPR/DMPO experiment is also conducted over pure CN in Fig. S19, no DMPO/*OH signals are detected under darkness or visible light illumination. While, for Fe(III)/Fe-CN sample, it can also be observed the DMPO/*OH signals under visible light irradiation, but the intensity of signal is weaker than Fe(III)/CQDs/Fe-CN. Hence, we could speculate the generation of *OH adduct is not via pure CN, but originated from IFCT effect. According to the above results, the possible processes of the generation of *OH adduct are illustrated below. As the IFCT effect that of grafted Fe(III), one parts of the excited electron could quickly transfer from VB of CN to Fe(III) and Fe(III) species could trap one electron to transform into a Fe(II) species (Fe(III)/Fe(II), 0.77 V, vs NHE). Consequently, the photo-induced carriers could be fast separated and left holes stay in the VB. And according to Nosaka et al. reported [38,43], as photo-induced hole existed, H₂O₂ could be produced from H₂O. Then, as the potential of *OH/H₂O₂ (1.07 V vs. NHE) is smaller than the VB of CN (1.57 eV vs. NHE), the obtained H₂O₂ could sequentially react with Fe²⁺ to form *OH (eqn (1) and (2)). This reaction is generally known as the Fenton reaction, indicating the Fe(III)/CQDs/Fe-CN catalyst would generate the photo-Fenton effect under visible light illumination without the extra addition of H₂O₂ which remarkably improves the photocatalytic activity. And at the same time, Fe(II) species is oxidized to

Fe(III) which retains the dynamic equilibrium of Fe(III)/Fe(II) under the visible light radiation.



Due to serve as the key role to form H₂O₂, the trapped of h⁺ by the addition ammonium oxalate (AO) could also inhibit the degradation of MO. Furthermore, the singlet oxygen radical ¹O₂ is also examined by EPR/TEMPO probe, it can be clearly observed a three-line spectrum with the intensity ratio of 1:1:1 in Fig. 8D, corresponding to the characteristic spectrum of TEMPO/1O₂. But ¹O₂ just plays a minor role in this reaction system, because the addition of the quencher, N₃⁻, just slightly reduced the photocatalytic performance. Therefore, combined with the above mentioned results, these demonstrate that *OH active species and h⁺ is the major oxidation species over Fe(III)/CQDs/Fe-CN in the degradation of MO.

4. Conclusions

In summary, carbon nanodots (CQDs) is successfully coupled with Fe-doped CN, which shows the enhanced visible light absorp-

tion region and yields the raised surface absorption active sites. Then grating of Fe(III) species into CQDs/Fe-CN composite exhibits the highly photocatalytic activity, ascribing to the largely promoted light absorption, the reduced transportation distance of photo-induced carriers by the interfacial charge transfer effect (IFCT) and also could be contributed to the generation of •OH active species by the photo-Fenton originated from grating Fe(III). This work demonstrated a simple way to combine iron species and carbon nanodots to modify the pure CN to construct the highly photocatalytic performed ternary photocatalysts by the introduction of the IFCT effect and the photo-Fenton effect.

Acknowledgement

This work was supported by the National Natural Science Foundation of China (No. 21276088 and 60976053)

Appendix A. Supplementary data

Supplementary data associated with this article can be found, in the online version, at <http://dx.doi.org/10.1016/j.apcatb.2016.12.028>.

References

- [1] A. Kudo, Y. Miseki, Chem. Soc. Rev. 38 (2009) 253–278.
- [2] X. Wang, K. Maeda, A. Thomas, K. Takanabe, G. Xin, J.M. Carlsson, K. Domen, M. Antonietti, Nat. Mater. 8 (2009) 76–80.
- [3] W.-J. Ong, L.-L. Tan, Y.H. Ng, S.-T. Yong, S.-P. Chai, Chem. Rev. 116 (2016) 7159–7329.
- [4] N. Sagara, S. Kamimura, T. Tsubota, T. Ohno, Appl. Catal. B: Environ. 192 (2016) 193–198.
- [5] J. Yan, H. Wu, H. Chen, Y. Zhang, F. Zhang, S.F. Liu, Appl. Catal. B: Environ. 191 (2016) 130–137.
- [6] X. Li, Y. Pi, L. Wu, Q. Xia, J. Wu, Z. Li, J. Xiao, Appl. Catal. B: Environ. 202 (2017) 653–663.
- [7] Y. Zheng, L. Lin, X. Ye, F. Guo, X. Wang, Angew. Chem. Int. Ed. 53 (2014) 11926–11930.
- [8] L. Ma, H. Fan, J. Wang, Y. Zhao, H. Tian, G. Dong, Appl. Catal. B: Environ. 190 (2016) 93–102.
- [9] L. Ma, H. Fan, M. Li, H. Tian, J. Fang, G. Dong, J. Mater. Chem. A 3 (2015) 22404–22412.
- [10] J. Zhang, G. Zhang, X. Chen, S. Lin, L. Möhlmann, G. Dolęga, G. Lipner, M. Antonietti, S. Blechert, X. Wang, Angew. Chem. Int. Ed. 124 (2012) 3237–3241.
- [11] J. Liu, Y. Liu, N. Liu, Y. Han, X. Zhang, H. Huang, Y. Lifshitz, S.-T. Lee, J. Zhong, Z. Kang, Science 347 (2015) 970–974.
- [12] X. Chen, J. Zhang, X. Fu, M. Antonietti, X. Wang, J. Am. Chem. Soc. 131 (2009) 11658–11659.
- [13] Q. Liu, J.Y. Zhang, Langmuir 29 (2013) 3821–3828.
- [14] G.D. Ding, W.T. Wang, T. Jiang, B.X. Han, H.L. Fan, G.Y. Yang, Chemcatchem 5 (2013) 192–200.
- [15] X.C. Wang, X.F. Chen, A. Thomas, X.Z. Fu, M. Antonietti, Adv. Mater. 21 (2009) 1609–+.
- [16] Y. Zheng, Y. Jiao, Y.H. Zhu, L.H. Li, Y. Han, Y. Chen, A.J. Du, M. Jaroniec, S.Z. Qiao, Nat. Commun. 5 (2014) 1–8.
- [17] Y. Zhao, F. Zhao, X.P. Wang, C.Y. Xu, Z.P. Zhang, G.Q. Shi, L.T. Qu, Angew. Chem. Int. Ed. 53 (2014) 13934–13939.
- [18] G. Gao, Y. Jiao, F. Ma, Y. Jiao, E. Waclawik, A. Du, Phys. Chem. Chem. Phys. 17 (2015) 31140–31144.
- [19] C. Creutz, B.S. Brunschwig, N. Sutin, J. Phys. Chem. B 109 (2005) 10251–10260.
- [20] C. Creutz, B.S. Brunschwig, N. Sutin, J. Phys. Chem. B 110 (2006) 25181–25190.
- [21] Q. Liu, Y.R. Guo, Z.H. Chen, Z.G. Zhang, X.M. Fang, Appl. Catal. B: Environ. 183 (2016) 231–241.
- [22] Q. Liu, T.X. Chen, Y.R. Guo, Z.G. Zhang, X.M. Fang, Appl. Catal. B: Environ. 193 (2016) 248–258.
- [23] Q. Han, B. Wang, Y. Zhao, C.G. Hu, L.T. Qu, Angew. Chem. Int. Ed. 54 (2015) 11433–11437.
- [24] H. Yu, H. Irie, Y. Shimodaira, Y. Hosogi, Y. Kuroda, M. Miyauchi, K. Hashimoto, J. Phys. Chem. C 114 (2010) 16481–16487.
- [25] M. Akçay, J. Mol. Struct. 694 (2004) 21–26.
- [26] S. Cao, J. Low, J. Yu, M. Jaroniec, Adv. Mater. 27 (2015) 2150–2176.
- [27] J. Moulder, J. Hammond, K. Smith, Appl. Surf. Sci. 25 (1986) 446–454.
- [28] R.M. Cornell, U. Schwertmann, The Iron Oxides: Structure, Properties, Reactions, Occurrences and Uses, John Wiley & Sons, 2003.
- [29] J. Han, A. Liu, J. Zhu, M. Tan, H. Wu, Appl. Phys. A 88 (2007) 341–345.
- [30] J. Chastain, R.C. King, J. Moulder, Handbook of X-ray Photoelectron Spectroscopy: a Reference Book of Standard Spectra for Identification and Interpretation of XPS Data, Physical Electronics, Eden Prairie, MN, 1995.
- [31] Y. Li, L. Machala, W.L. Yan, Environ. Sci. Technol. 50 (2016) 1190–1199.
- [32] M. Liu, X.Q. Qiu, M. Miyauchi, K. Hashimoto, J. Am. Chem. Soc. 135 (2013) 10064–10072.
- [33] X.Q. Qiu, M. Miyauchi, K. Sunada, M. Minoshima, M. Liu, Y. Lu, D. Li, Y. Shimodaira, Y. Hosogi, Y. Kuroda, K. Hashimoto, Acs Nano 6 (2012) 1609–1618.
- [34] W.B. Sun, H.Y. Zhang, J. Lin, J. Phys. Chem. C 118 (2014) 17626–17632.
- [35] D.D. Zheng, C.Y. Pang, Y.X. Liu, X.C. Wang, Chem. Commun. 51 (2015) 9706–9709.
- [36] M. Nishikawa, R. Takanami, F. Nakagoshi, H. Suizu, H. Nagai, Y. Nosaka, Appl. Catal. B: Environ. 160 (2014) 722–729.
- [37] Y. Nosaka, M. Nishikawa, A.Y. Nosaka, Molecules 19 (2014) 18248–18267.
- [38] M. Nishikawa, Y. Mitani, Y. Nosaka, J. Phys. Chem. C 116 (2012) 14900–14907.
- [39] J.S. Zhang, M.W. Zhang, L.H. Lin, X.C. Wang, Angew. Chem. Int. Ed. 54 (2015) 6297–6301.
- [40] T.Y. Ma, J.L. Cao, M. Jaroniec, S.Z. Qiao, Angew. Chem. Int. Ed. 55 (2016) 1138–1142.
- [41] H.T. Li, X.Y. Zhang, D.R. MacFarlane, Adv. Energy Mater. 5 (2015).
- [42] Y.J. Cui, Z.X. Ding, P. Liu, M. Antonietti, X.Z. Fu, X.C. Wang, Phys. Chem. Chem. Phys. 14 (2012) 1455–1462.
- [43] J. Zhang, Y. Nosaka, J. Phys. Chem. C 117 (2013) 1383–1391.